ACS APPLIED MATERIALS & INTERFACES

Research Article

Cite This: ACS Appl. Mater. Interfaces XXXX, XXX, XXX−XXX

www.acsami.org

Porous Biomimetic Hyaluronic Acid and Extracellular Matrix Protein Nanofiber Scaffolds for Accelerated Cutaneous Tissue Repair

Christophe O. Chantre,[†,‡] Grant M. Gonzalez,[†] Seungkuk Ahn,[†] Luca Cera,[†] Patrick H. Campbell,[†] Simon P. Hoerstrup,[‡] and Kevin Kit Parker*[,†]

[†]Disease Biophysics Group, Wyss Institute for Biologically Inspired Engineering, John A. Paulson School of Engineering and Applied Sciences, Harvard University, Cambridge, Massachusetts 02138, United States

[‡]Institute for Regenerative Medicine, University of Zurich, Zurich 8044 ZH, Switzerland

Supporting Information

ABSTRACT: Recent reports suggest the utility of extracellular matrix (ECM) molecules as raw components in scaffolding of engineered materials. However, rapid and tunable manufacturing of ECM molecules into fibrous structures remains poorly developed. Here we report on an immersion rotary jet-spinning (iRJS) method to show high-throughput manufacturing (up to ∼1 g/min) of hyaluronic acid (HA) and other ECM fiber scaffolds using different spinning conditions and postprocessing modifications. This system allowed control over a variety of scaffold material properties, which enabled the fabrication of highly porous (70−95%) and water-absorbent (swelling ratio ∼2000−6000%) HA scaffolds with soft-tissue mimetic mechanical properties (∼0.5−1.5 kPa). Tuning these scaffolds' properties enabled the identification of porosity (∼95%) as a key facilitator for rapid and in-depth cellular ingress in vitro. We then demonstrated that porous HA scaffolds accelerated granulation tissue formation, neovascularization, and reepithelialization in vivo, altogether potentiating faster wound closure and tissue repair. Collectively, this scalable and versatile manufacturing approach enabled the fabrication of tunable ECM-mimetic nanofiber scaffolds that may provide an ideal first building block for the design of all-in-one healing materials.

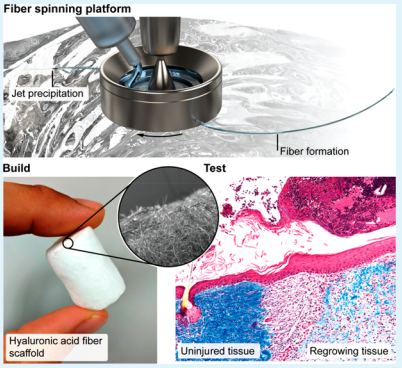

KEYWORDS: *hyaluronic acid, biomimetic, porosity, immersion rotary jet spinning, nanofiber, wound healing, regeneration*

INTRODUCTION

Cutaneous wound healing is a reparative and protective mechanism aimed at efficiently restoring tissue integrity and homeostasis. Severe wounds and chronic ulcers may potentiate adverse and even life-threatening complications (such as septicemia or amputations[1]). In this case, wound healing is achieved by the formation of a fibrotic tissue, known as a scar.[2,3] Scars represent maladaptive processes, can result in undesirable aesthetic appearance, and cause traumatic psychological sequelae.[4] Chronic nonhealing wounds are stalled in the healing process and are unable to achieve tissue closure.[5] To address this problem, regenerative medicine approaches have emerged to support functional and cosmetic restoration of damaged or diseased tissues.[3,6] State-of-the-art wound dressings are now being designed as instructive materials aimed at supporting and stimulating a regenerative response by the host.[7] By functionalizing these materials with morphogenic cues and tailoring them to recapitulate the key biophysical and biochemical properties of target tissues, considerable improvements over standard treatments have already been reported.[8,9] Several parallel approaches are currently being advanced to design these materials, using plant, synthetic, or biologic sources, to establish the first building block of these instructive systems.[10]

Natural biological materials, such as extracellular matrix (ECM) molecules, present a unique advantage for designing wound dressings as they evolved to directly interact and function with cells and tissues. In vivo, these ECM materials are found as proteins and glycosaminoglycans (GAGs), are weaved into fibrillar structures and meshes, and provide physical support and regulatory function.[11] Their structural and mechanical properties can furthermore bestow these molecules with significant influence over specific cell behaviors, critical to homeostasis, wound healing, and regeneration.[12] The GAG hyaluronic acid (HA) in particular has received considerable attention for its regulatory roles during development[13] and in several regenerative phenomena observed in mice,[14] fish,[15] amphibians,[16] and human fetal skin.[17] Its inherent biocompatibility, mechanical and structural tunability, and water-retention properties have also made HA a promising candidate for tissue engineering applications.[18] The availability of reactive functional groups along its disaccharide chain have also been leveraged for functionalization with morphogenic compounds,[19] matrix metalloproteinases,[20] and cell-binding moieties.[21] Taking

Received: September 24, 2019
Accepted: November 11, 2019

DOI: 10.1021/acsami.9b17322
ACS Appl. Mater. Interfaces XXXX, XXX, XXX−XXX

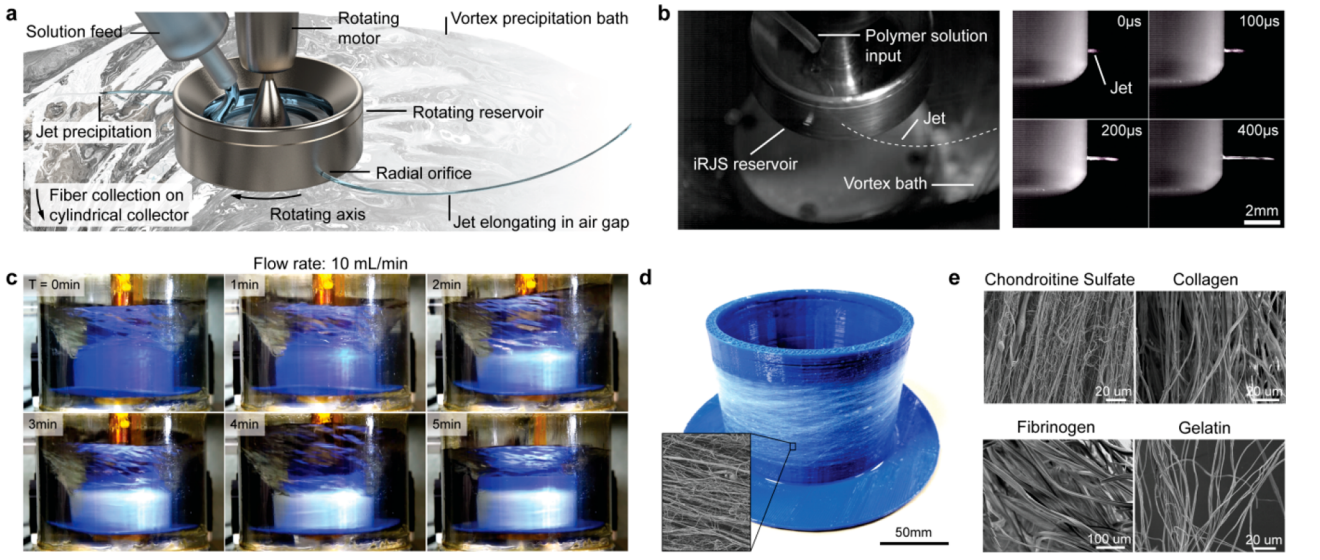

Figure 1. High-throughput production of biological nanofiber scaffolds using an immersion rotary jet-spinning (iRJS) platform. (a) Schematic of the iRJS system with (b) corresponding still images of the reservoir rotating at 15k rpm and spinning an HA solution. The iRJS is designed with a perforated rotating reservoir, capable of spinning at up to 60k rpm, and a vortex precipitation bath positioned axially to the reservoir. The high centrifugal forces exerted by the spinning reservoir will drive extrusion of the polymer dope out of the reservoir through the two radial orifices, forming a jet that will elongate across the air gap before hitting the vortex precipitation bath. Fiber formation and collection around a cylindrical collector will ensue. (b) Still images taken using a high-speed camera depicting jet elongation from ~0 s to 400 μs after jet initiation. (c) Side-view images of the whole iRJS setup at different spinning time points (0−5 min), emphasizing the high-throughput capabilities of the system, where HA fibers (in white) are collected on a collector (blue) in the precipitation vortex bath. (d) Centimeter-wide sheet of fibers wrapped around a collector. Inset shows scanning electron micrograph of fibers with a nonwoven alignment organization. (e) To demonstrate the versatility of our manufacturing approach, the GAG chondroitine sulfate and the ECM proteins collagen, fibrinogen, and gelatin were used to fabricate micro- and nanofiber scaffolds from aqueous solutions. SEM images are shown.

advantage of such approaches enabled the development of HA-based scaffolds that supported tissue repair of healthy and diabetic skin tissues,[22,23] while pure HA dressings have already found use in the clinic.[24] The full potential of these strategies may however remain unrealized because of their oversimplified biomimetic properties, lacking the temporal and spatial complexity[6,25] required to guide efficient cellular integration and tissue regeneration.

To improve recapitulation of the structural and topographical features of the native ECM, micro- and nanofiber scaffolds have emerged as an efficacious approach and have contributed to the development of a variety of biomimetic pro-regenerative materials.[26−28] Their characteristic porous architecture and fiber directionality can facilitate integration and adaptive remodeling within the host tissue (for example, in vascular grafts[29]). To date, several spinning methods (such as electrospinning[30] and wet-spinning[31]) exist for manufacturing these fibrous scaffolds with relative versatility. These methods, however, present biological and engineering design constraints when it comes to producing pure ECM fibers[32,33] at scales that can foster preclinical development and subsequent clinical translation.[34] Small pore sizes resulting from tight packing of nanoscale fibers has emerged as a common hindrance of these fibrous scaffolds.[35] They typically offer limited cellular ingress as well as low gas and nutrient diffusion,[36] which is critical in the absence of an embedded vasculature.[37] Complementary strategies focused on increasing the porosity via enzymatically controlled degradation,[38] sacrificial components,[39] or expansion methods[40] have therefore been developed but present additional steps and complexity in the fabrication process. In the context of HA fiber manufacturing, spinning methods have also typically required carrier polymers,[41] high temperatures,[42] or added air-blowing systems to facilitate fiber formation,[43] because high viscosity, hydrophilicity, and surface tension can hinder manufacturability.[44] To address these shortcomings, we previously introduced the development of an immersed rotary jet-spinning (iRJS) system[45]—a modified version of the original RJS,[46] which utilized high centrifugal forces to elongate protein and polymer jets into nanofiber structures. The high production rates of this original RJS system (in grams per minute) facilitated the rapid manufacture of tissue-engineered heart valves,[47] pro-regenerative wound dressings,[27,28] and lab-grown meat analogues.[48] The new immersed RJS (iRJS) system is integrated with a vortexed precipitation bath that overcomes the need to rely on volatile carrier solvents to evaporate for fiber formation. Surface tension instabilities (mediated by specific solution viscosities and solvent evaporation rates) that can accelerate fiber breakage and beading are significantly reduced in this system, thus enabling the production of a diverse set of new materials and spinning conditions.[45] As such, we reasoned that an iRJS system should readily support the manufacture of HA nano- and microfibers, encompassing a broad parameter spectrum, which is advantageous for designing instructive and biomimetic wound dressings.

In this study, we showed high-throughput manufacture of pure HA into fibrous hydrogel scaffolds from aqueous solutions, thus eliminating the requirement for volatile solvents or polymeric carrier adjuvants. This in turn allowed the fabrication of a variety of material properties using different spinning conditions. We then focused on the design of ultrasoft and stable tissue-mimetic wound dressings, with high porosity and water absorbency—properties typically unattainable using traditional spinning methods.[49] Experiments performed in vitro highlighted in particular the advantage of such high porosity, illustrated by

DOI: 10.1021/acsami.9b17322
ACS Appl. Mater. Interfaces XXXX, XXX, XXX−XXX

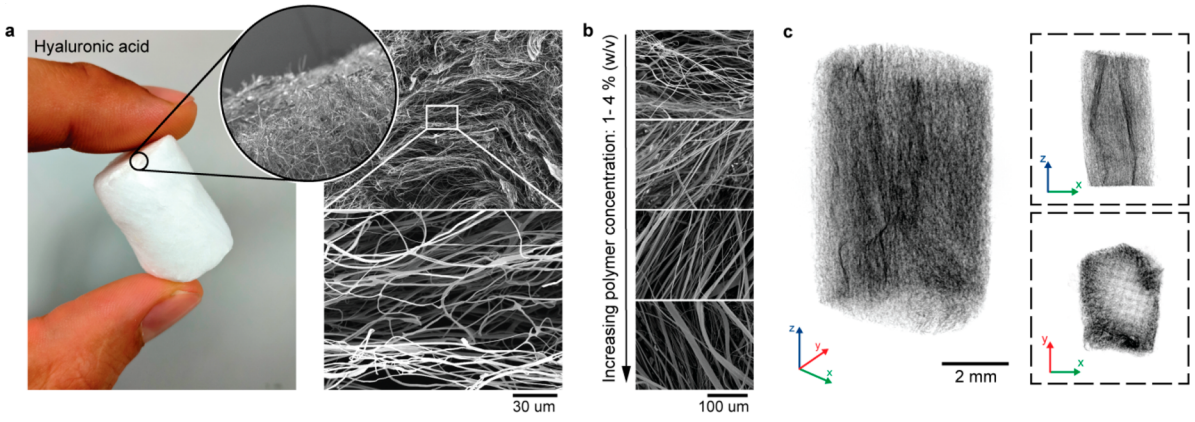

Figure 2. Versatile spinning conditions of porous nanofiber HA scaffolds. (a) Large nanofiber scaffolds were produced in a single-step process using a range of concentrations (1−4% weight/volume) from aqueous solutions. (Left) Macroscopic image showing a HA scaffold lyophilized into a cylindrical shape. (Right) Scanning electron micrographs (SEMs) depict the typical nonwoven structure produced using our collectors. (b) SEMs of different HA scaffolds produced using increasing concentrations (w/v) of HA in the starting aqueous solution. (c) Large scaffolds could additionally be imaged using μCT, detailing the uniform fibrous and porous structure throughout the scaffold. In the cross-sectional rendering, the increased fiber density on the surface is caused by scaffold collapse during lyophilization.

the rapid and in-depth cellular permeation of dermal fibroblasts. In vivo experiments then enabled investigation of the regenerative potency of these HA scaffolds in mice, which revealed faster granulation tissue formation, neovascularization, and reepithelialization than in nontreated controls. Comparing scaffolds of varying porosity additionally reaffirmed the importance of appropriately tailoring structural properties for such indications. Altogether, this study demonstrated the use of a rapid process for fabricating HA and other ECM molecules into nanofiber scaffolds, as well as how their assembly into biomimetic and porous structures supported tissue repair.

RESULTS

Production-Scale Manufacture of ECM Micro- and Nanofibers Using iRJS. We previously reported that RJS could fabricate a variety of natural, synthetic, or biological polymers with tunable fiber size and mechanics.[27,46,47,50,51] In the new immersed RJS (iRJS), the addition of a precipitation bath, commonly used in traditional wet-spinning setups,[31] further expanded the versatility of the technology, thus enabling the manufacture of several novel materials, including alginate or DNA.[45] We hypothesized that this system could be further leveraged into fabricating a wide range of biologically sourced and highly tunable fiber scaffolds, relevant for the design of functional tissue engineering and regenerative medicine materials.

To process these biological materials into fibers, the combination of a water-based solvent, a strong centrifugal force, and an ethanol precipitation bath is here exploited. Specifically, in an automated iRJS setup, a polymer solution is continuously channeled in the rotating reservoir, accelerated through two 500-μm-wide orifices via high centrifugal forces, and ejected across an air gap and into a precipitation bath (Figure 1a and b and Figure S1a). As the polymer jet hits the precipitation bath, the solvent rapidly dissipates, leaving an aggregated and stable fiber whirling in the vortex.[45] The polymer fiber then gradually and continuously wraps around a cylindrical collector (in blue), forming a nonwoven thick sheet (in white) (Figure 1c and d and Movie S1; images here are shown with hyaluronic acid fibers). A 5-L vortexed precipitation bath and a large cylindrical collector enabled the manufacture of centimeter-wide thick fiber scaffolds.

To first illustrate the versatility of this approach, we investigated the fabrication of several different ECM proteins and GAGs. Typically, engineering biological fibers has been enabled or enhanced by using synthetic carrier polymers (such as polycaprolactone or polyethylene glycol) that facilitate fiber formation.[50] Although incorporation of such materials may prove critical in certain applications where, for example, superior mechanical properties are required (i.e., tissue-engineered heart valves[47] and ventricles[52]), designing entirely biological fibrous materials remains relevant for a variety of regenerative medicine applications.[10,53,54] The GAG, chondroitin sulfate (CS), two ECM proteins—fibrinogen and collagen type I, and gelatin, the denatured form of collagen, were all spun directly from aqueous solutions. Scanning electron micrographs (SEMs) reveal the formation of fibrous structures for all these materials (Figure 1e), and higher-magnification micrographs detail their surface topography (Figures S1b and S2). A range of polymer concentrations and blends was furthermore amenable to fiber formation (Figure S2), as detailed in Table S1.

To demonstrate the high-throughput capability of this platform and the tunability of the scaffolds, we focus on the production of hyaluronic acid (HA). Notably, fabrication of HA nanofiber scaffolds using a benchtop system was possible at production rates 2−4 times higher than in comparable electrospinning systems[43] and was on the same order of magnitude as high-throughput commercial systems.[55] Further increasing the throughput could nonetheless be achieved by transitioning to a continuous collection system and increasing the amount of nozzles in the spinning reservoir. In addition, whereas previous publications described the fabrication of pure nanoscale HA fibers,[43,56] our method supports nanofiber manufacturing with a range of polymer concentrations (from 1 to 4%) that could be consistently spun into uniform and robust scaffolds (Figure 2a and b and Movie S2). This broad range of polymer concentration is potentiated by a reduced reliance on traditional spinning parameters (dope concentration and solution viscosity). The introduction of a precipitation bath abbreviated the jet-elongating time scale (compared to dry-jet-spinning or electrospinning), thus limiting potential beading

DOI: 10.1021/acsami.9b17322
ACS Appl. Mater. Interfaces XXXX, XXX, XXX−XXX

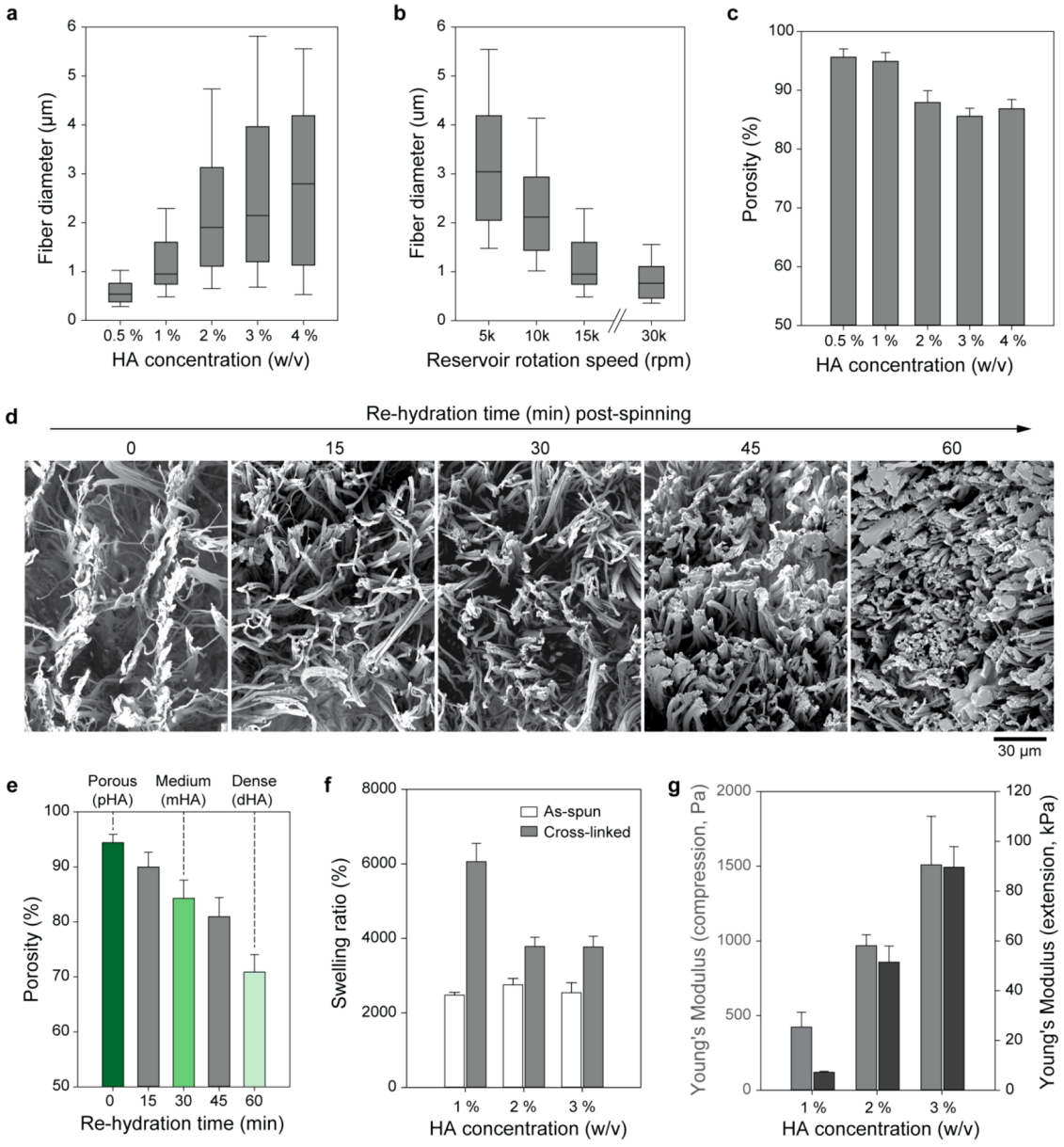

Figure 3. HA scaffolds demonstrate structural and mechanical tunability. (a) Fiber diameter increases from ~500 nm for 0.5% (w/v) HA polymer dope to ~3.0 μm for the 4% for fixed spinning at 15k rpm. (b) Fiber diameter conversely decreases with reservoir rotation speed increase, reaching average diameters below 1.0 μm at 15k rpm and above. (c) Porosity measurements reveal porous structures averaging between 85 and 95% depending on HA dope concentration. (d) Porosity could be modulated more significantly, and without relying on polymer dope, via rehydration (or fiber dissolution) postspinning. SEM cross section images of five different scaffold porosities that were enabled by rehydrating the scaffolds for 0, 15, 30, 45, and 60 min. (e) Corresponding data show that as-spun (maintained in a dehydrated state) HA scaffolds (1% w/v) have a porosity of ~95%, while scaffolds exposed to air for 60 min exhibit a porosity of ~70%. Porous (pHA), standard (sHA), and dense (dHA) nomenclature are used for subsequent experiments. (f) As-spun scaffolds demonstrate a strong water absorption capacity (calculated as the swelling ratio), reaching a ~25−30-fold increase (2 500%−3 000%) in weight from their dry state. Water absorption capacity increased post-cross-linking, reaching 60-fold increase in weight (~6 000%) for the 1% HA scaffolds. (g) Young's modulus in compression and in extension (along fiber axis) scale with HA concentration, suggesting a correlation with fiber diameter detailed in (a). (a, b) n = 3 sample runs per condition with 4−6 fields of view (FOVs) each. (c, e) n = 6 samples per condition. (f) n = 8 samples per condition. (g) n = 5−8 samples per condition. Box plots with edges, middle bars, and whiskers represent 25th and 75th percentiles, median, and fifth and 95th percentiles, respectively. Errors bars in bar graphs are presented as s.e.m.

generated by surface tension instabilities.[45] Additionally, the use of high centrifugal forces, causing shear strain rates of 1000 s^{-1} or above in the reservoir channel,[28] decreased dependency on solvent viscosity—a common hindrance of traditional spinning[57] or 3D-printing techniques.[58] This was confirmed with rheological measurements of HA dopes that revealed shear-thinning behaviors, where viscosity curves significantly decreased at high shear rates and showed convergent trajectories for all different concentrations (Figure S3). Thus, beading, or fiber breakage, could be reduced for a variety of dope concentrations, while spinning capabilities were retained or even increased.

The uniform porous and fibrous structure that was achieved throughout the scaffolds is exemplified by an SEM image taken at the center of a centimeter-thick scaffold (Figure S4) and X-ray micro computed tomography (μCT) renderings (Figure 2c).

DOI: 10.1021/acsami.9b17322
ACS Appl. Mater. Interfaces XXXX, XXX, XXX−XXX

While an increase in fiber density on the surface is observed, likely caused by scaffold collapse during lyophilization, these renderings nonetheless enable to demonstrate the maintenance of a highly porous architecture over several millimeters of scaffold. Collecting fibrous materials at this size scale readily addresses limitations of previously tested electrospinning systems for manufacture of HA[56] as well as other materials.[59] Indeed, in these systems the electrical fields required for jet elongation and subsequent fiber formation can accumulate on thicker samples, thus impeding uniform assembly[59] and leading to heterogeneous structures.[56] Rapid fabrication of such thick scaffolds, while retaining their inherent porous nature, may become increasingly relevant if these scaffolds are considered for large-surface-area wounds.

Investigating and Tuning Fiber Structure and Mechanics. The architectural and biophysical properties are, along with a microenvironment's unique biochemical makeup, critical mediators of tissue function and regeneration.[6−8] Designing potent proregenerative scaffolds must therefore require the ability to tailor these specific properties, whether mechanical or structural, to a specific organ for optimal integration and subsequent regenerative instruction. Following this reasoning, we previously reported the development of dermal ECM-mimetic fibrous materials, sourced from both plant[27] and biological[28] materials, to accelerate wound closure and stimulate endogenous repair.

To test these biomimetic and instructive material properties, we focused here on hyaluronic acid fiber scaffolds. First, we confirmed that iRJS induced HA assembly into fibrous, internally aligned structures (Figure S1b), often observed in ECM proteins in vivo.[11] Individual fibers ranged on average from ∼500 nm to ∼3 μm for dope concentrations of 0.5−4.0% weight/volume (w/v) (Figure 3a), with an increase in size distribution evident with increasing HA concentrations. This was likely caused by the higher viscosities of these solutions (Figure S3), thus limiting their ability to continuously flow in the spinning reservoir and creating instabilities during jet elongation. The low viscosity of the 0.5% HA may conversely explain its higher sensitivity in achieving optimal spinnability. Finally, varying reservoir speed rotation, which modulates the shear forces that form the polymer jet,[28] likewise modified fiber diameter (Figures 3b and S5), corroborating previous observations.[45]

We next investigated the porosity of these HA scaffolds, as tissue integration can be severely hampered by minimally porous micro- or nanofiber scaffolds.[39] We measured porosities between 85 and 95% for all our tested conditions (Figure 3c), contrasting the significantly lower percent range (40−55%) of dry-spinning techniques[47] (such as RJS or electrospinning; see Figure S6). We believe that the collection method—a wet rotating bath—supports an uncompressed scaffold assembly and concomitantly prevents fiber bonding, which may occur in traditional dry-spinning setups.[39] We also observed that fiber sheets taken out of the precipitation solution and exposed to air at room temperature and prior to further storage or postprocessing exhibited decreased porosities (Figure 3d). Regarding this effect, we measured a dependency with time, as porosities could be significantly reduced with drying times of 15 min or above, while other parameters remained unchanged (Figure 3d and e). The faster evaporation of ethanol compared to that of water in the precipitation solution[60] (80% ethanol/20% water) likely caused a gradual increase in water content. Because water acts as a solvent for HA, rehydration caused fibers' surfaces to gradually merge together and, therefore, decreased scaffold porosity. This process was then halted by resubmerging the scaffolds in a precipitation solution.

Water-absorbent dressings have demonstrated the capability of removing wound exudates, while providing a hydrated environment for cell viability and growth.[56] As such, the swelling ratios of 1−3% HA scaffolds were measured—chosen for the proceeding measurements because of their optimal spinnability. They exhibited highly absorbent properties (∼1500−3000%) within minutes of water contact (Figures 3f and S8). For comparison, this is an order of magnitude higher than our previous cellulose-based fiber scaffolds that supported tissue restoration in a murine model.[27] Prolonged measurements, however, revealed a rapid degradation of their fibrous architecture, indicative of non-cross-linked HA polymer chains. Using well-established protocols, ester bond formations were induced via an *N*-ethyl-*N*′-(3-(dimethylamino)propyl)-carbodiimide (EDC)/*N*-hydroxysuccinimide (NHS) catalyst, condensing the hydroxyl- and carboxyl-groups of the HA molecule[61] via esterification, thus significantly decelerating degradation kinetics (Figure S7). After a week, the scaffolds still retained 80% or more of their initial weight. Concomitantly, we observed an increase in water absorbance for these cross-linked scaffolds, reaching a ratio close to 6000% for the 1% HA samples (Figure 3f). Fiber diameter and porosity were, however, minimally affected by this cross-linking process (Figure S8).

Mechanical properties finally demonstrated stiffness regimes on par with mammalian soft tissue mechanics,[62,63] theoretically a prerequisite for biomimetic scaffold design. Measurements were performed in compression and extension (along the fiber axis), exhibiting Young's moduli ranging from ∼450 to 1 500 Pa (in compression) and ∼5 to 100 kPa (in extension) (Figure 3g). While mechanical tests perpendicular to the fiber axis (in extension) were attempted, the soft and anisotropic nature of the scaffolds caused them to rapidly tear, making data collection unreliable. Mechanical tests, however, did reveal that scaffold stiffnesses were significantly influenced by fiber size, as indicated by the higher values with increased HA concentrations. Manual stretching of fiber bundles showed elastic behaviors typically observed in hydrogel materials (Movies S3 and S4), which may integrate well with the viscoelastic properties of native tissues.[64] Moving forward, scaffolds of 1% HA were chosen for functional testing based on their desired biomimetic properties, which included low-micron-range fiber size and low mechanical properties.[7] High porosity and water absorbency were also considered additional benefits of this spinning condition.

Highly Porous HA Scaffolds Enable Direct Cellular Permeation. We exploited the ability to manipulate HA scaffold properties to investigate the influence of porosity on cell penetration upon seeding. We hypothesized that highly porous scaffolds should enable rapid ingress of cells, when compared to denser scaffolds that are more representative of existing proregenerative fibrous materials (<60%).[47,59] Three different groups were tested in an in vitro assay and were termed as follows: porous HA (pHA: ∼95% porosity, 0 min rehydration), medium HA (mHA: ∼85% porosity, 30 min rehydration), and dense HA (dHA: ∼70% porosity, 60 min rehydration). Other parameters were kept unchanged (precursor solution of 1% HA spun at 15k rpm) with fibers in the ∼1 μm range, low stiffness regimes, and high water absorbency (Table 1; see Figure 3 for details).

In this assay, HA scaffolds of ∼0.5 mm in thickness and 6 mm in diameter were seeded with green fluorescent protein (GFP)-

DOI: 10.1021/acsami.9b17322
ACS Appl. Mater. Interfaces XXXX, XXX, XXX−XXX

Table 1. Manufacturing Parameters for Designing HA Fiber Scaffolds of Varying Porosity

tested scaffold	dope concentration	spinning speed (rpm)	rehydration (min)	porosity (%)
dense HA (dHA)	1% HA	15k	60	~70
medium HA (mHA)	1% HA	15k	30	~85
porous HA (pHA)	1% HA	15k	0	~95

human neonatal dermal fibroblasts (GFP-HNDF) and tracked under live confocal microscopy 30 min following seeding. Observations with images at varying depths and 3D reconstructions confirmed the hypothesized influence of porosity on cellular permeation (Figure 4a and b). Dermal fibroblasts in the dense dHA scaffolds were constrained to the surface, where a compact network of fibers likely acted as an almost impermeable barrier to entry. Here, cell migration would be required to invade the scaffolds. Intensity measurements supported these observations, evident by a rapid decrease of signal 15 μm deep (Figure 4c), thus corroborating previous infiltration studies on nanofiber scaffolds.[47] In contrast, the more porous mHA scaffolds allowed penetration of cells in the sample, while the highly porous pHA supported a close to homogeneous diffusion of cells through >100 μm of scaffold (Figure 4b and c). Quantification of the average penetration (based on intensity values) and the penetration at the 100 μm depth position further revealed higher values for the pHA scaffolds when compared to the other conditions (Figure 4d). These data reveal how scaffolds may have significantly different effects upon implantation and underscore the importance of porosity.

To investigate how cells responded to these HA scaffolds, dermal fibroblasts were next cultured for 24 h and 7 days, tested for a lactate dehydrogenase (LDH) assay (Figure S9), and immunostained for cytoskeleton actin (Figure 4e and f). The LDH assay confirmed the biocompatibility of these HA scaffolds, characterized by no LDH release difference between the scaffolds and controls (no scaffold). The confocal images next revealed that the cells retained a rounded shape with

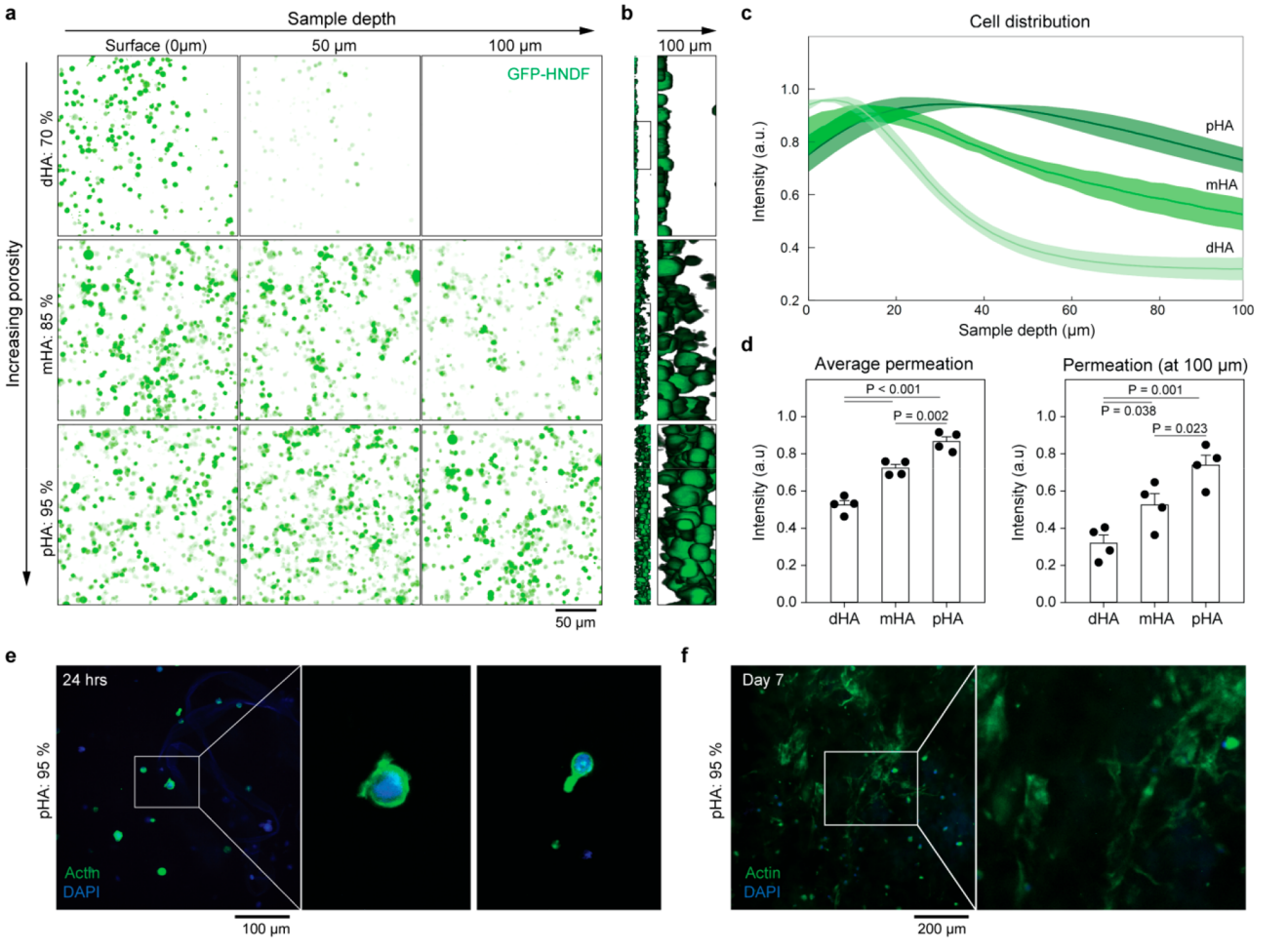

Figure 4. Cell permeation improves with increasing HA scaffold porosity. (a) Representative live-confocal microscope images of dermal fibroblasts (GFP-HNDFs) at the scaffold surface, 50 μm deep, and 100 μm deep for varying scaffold porosities (dense HA (dHA), 70%; medium HA (mHA), 85%; and porous HA (pHA), 95%). Precursor solution (1% w/v) spun at 15k rpm was used for all fabricated scaffolds. (b) Orthogonal views of 3D reconstruction, corresponding to images in (a). (c) Intensity values (normalized) were plotted up 100 μm in depth and confirm the decreased presence of cells deeper in the dHA and mHA scaffolds. (d) Quantification of cell numbers (intensity values) averaged over 100 μm (left) and measured at the 100 μm position (right) demonstrate significant differences between all groups tested. $n = 4$ samples with 4–6 FOVs per sample. One-way ANOVA with post hoc multiple comparisons Holm–Sidak's tests were performed. Significance was considered for $p < 0.05$. Errors bars are presented as s.e.m. (e, f) Confocal immunostaining of HNDFs cultured for 24 h (e) and 7 days (f) in a pHA scaffold.

DOI: 10.1021/acsami.9b17322
ACS Appl. Mater. Interfaces XXXX, XXX, XXX–XXX

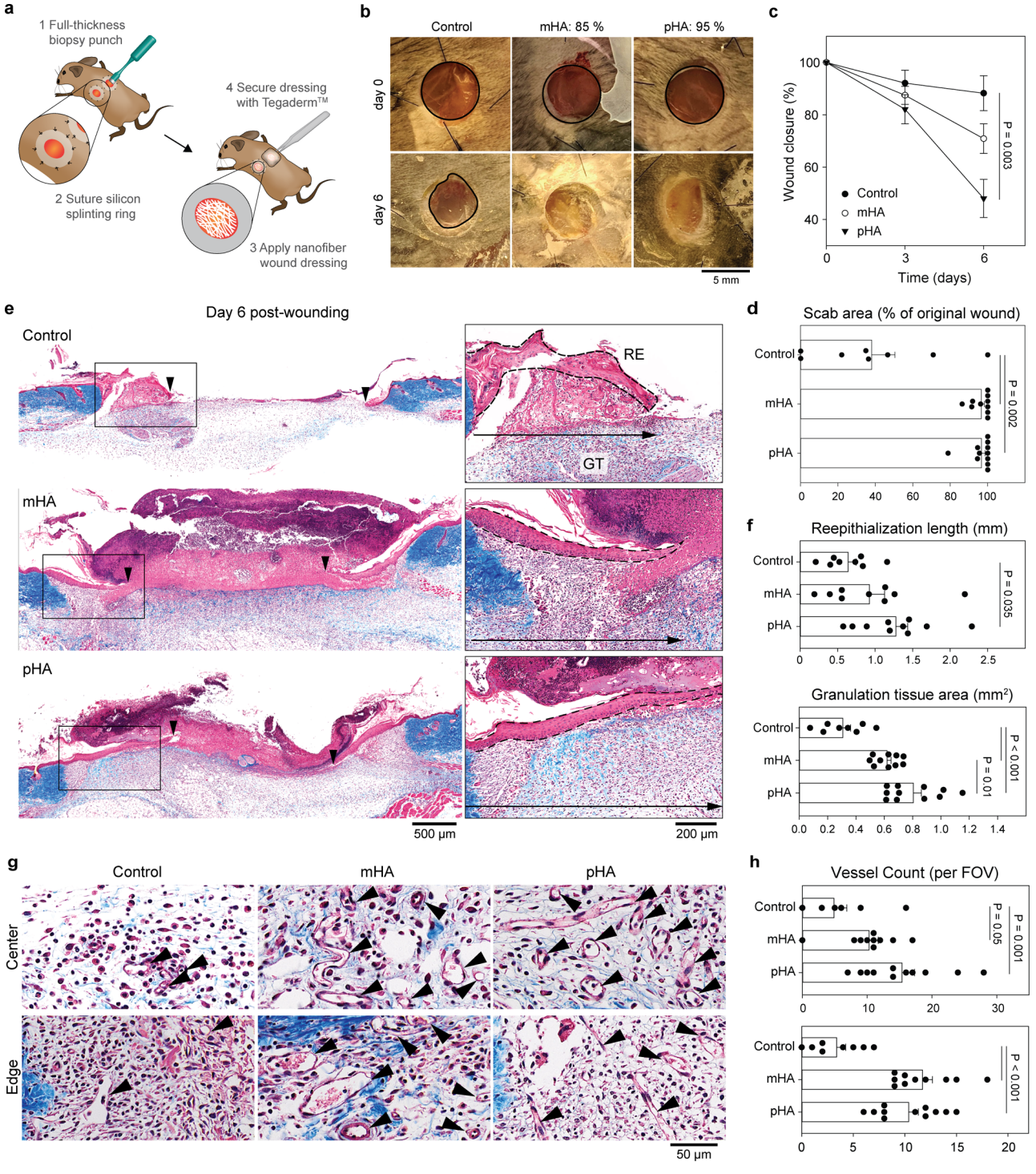

Figure 5. Porous HA scaffolds support robust wound closure and tissue regrowth. (a) Schematic of the full-thickness excisional splinting wound model procedure steps: (1) 6 mm full-thickness excisional wounds are inflicted on C57BL/6 male mice (8−10 weeks old), (2) silicon rings are sutured to the surrounding uninjured skin, (3) HA wound dressings are applied to the wound, and (4) silicon occlusive dressings (Tegaderm) are used to cover the wounds. (b) Representative macroscopic images of wounds at day 0 and day 6 post-injury for the control (only covered with a Tegaderm film dressing), mHA, and pHA dressings. HA-treated wounds reveal formation of a scab across the entire wounded area, while controls appear still completely open. (c) Wound closure as a percentage of the original wound area. $n = 5–8$ wounds per condition. (d) Scab area as a percentage of the original wound area 6 days after wounding. (e) Trichrome stained sections of control (top), mHA (center), and pHA (bottom) dressings at day 6 postwounding. Controls revealed minimal wound closure, characterized by the lack of reepithelialization. The center of the wound exhibited almost no cellular presence (see inset image). By contrast, both HA scaffolds demonstrated strong tissue regrowth, with the pHA group showing a significant difference in reepithelialization when compared to the control (see arrowheads and inset images). Both HA scaffolds supported granulation tissue formation bellow the epidermis (in blue). Black line surrounds remnant HA scaffolds infiltrated by host immune cells. Black dotted lines and arrows highlight formation of epithelial tongue and new epidermis. (f) Quantification of reepithelialization length (top) and granulation tissue formation (bottom) 6 days after wounding. (g) High-magnification histology images identifying blood vessels in the granulation tissue. Images are shown for areas at the center of the wounds and at the edges. Black arrowheads point to vessels. (h) Blood vessel count based on fields of view (FOVs) at center

DOI: 10.1021/acsami.9b17322
ACS Appl. Mater. Interfaces XXXX, XXX, XXX−XXX

Figure 5. continued

(top) and edges (bottom) of wounds 6 days after wounding. One-way ANOVA on ranks with post hoc multiple comparisons Holm−Sidak's tests were performed for b, f, h and a post hoc multiple comparisons Dunn's test was used for d. Significance was considered for $p < 0.05$. Errors bars are presented as s.e.m. RE, reepithelialization; GT, granulation tissue.

protrusions reaching out from their bodies after 24 h in culture (Figure 4e). Such cell morphologies are likely caused by the soft scaffold mechanics and their limited ability to form focal adhesion complexes on HA molecules.[13] After 7 days, cells started to invade the scaffold and showed more elongated morphologies, while some maintained their rounded shapes (Figure 4f). Together, these data suggest HA scaffolds' ability to rapidly integrate in a tissue and subsequently support tissue growth.

Accelerated Tissue Integration and Repair through Increased Scaffold Porosity. We next hypothesized that these porous HA (pHA) scaffolds should potentiate rapid tissue integration and subsequent tissue repair when tested in vivo. mHA scaffolds were used as the denser controls, despite being as porous, or more so, than materials fabricated using other spinning techniques.[41−43] Three different groups were tested on full-thickness wounds (6 mm in diameter) in mice, following established excisional splinting protocols that prevent tissue contraction to better replicate human cutaneous healing by secondary intention:[65] (1) pHA, (2) mHA wound dressings, and (3) nontreated controls. All wounds were covered with a Tegaderm film dressing to secure nanofiber scaffolds and limit entry of external pathogens (Figure 5a).

Macroscopically, both HA-treated wounds exhibited faster wound closure and formation of scabs 4−6 days post-wounding, contrasting the slower healing progress of nontreated controls (Figure 5b)—expected outcomes for splinted wounds.[65] To confirm these observations, quantification of the wound-closure rate was calculated (Figure 5c), revealing faster closure in particular for the pHA scaffolds. Scab tissues, which typically form over wounds to protect and support them heal, were also well-developed for HA treatments (Figure 5b and d). Long-term tracking of wound closure for a subset of mice revealed, however, that all wounds closed within a similar time frame (Figure S10). Histological analysis via trichrome staining at day 6 further revealed differences in wound morphologies (Figure 5e). pHA and mHA demonstrated reepithelialization (in red, highlighted with arrows), while formation of granulation tissue was apparent in the wounded areas. Quantification of the ongoing reepithelialization at day 6 displayed an improved trend for the two HA treatments, with a significant difference measured between the control and the pHA specimen (Figure 5f, top). Low amounts of remnant HA in and over the wounds, identified by Alcian blue staining, revealed efficient integration and concomitant biodegradation (Figure 5e and Figures S11−S13). The differences in granulation tissue formation between the different groups tested further suggested the role of these scaffolds in supporting neogenesis of dermal tissues prior to biodegradation (Figure 5e, bottom) and heralded porosity as an important regulatory property. Nontreated wounds by contrast showed less advanced reepithelialization and smaller areas of scab and granulation tissue formation, mirroring previous studies using excisional splinting models.[22] These preliminary data are promising and underscore how changes in the material structural properties—here the scaffold's porosity—can influence wound healing and tissue formation.

Finally, because neovascularization is a crucial process for supporting granulation tissue formation and wound closure,[2,3] we sought to quantify the amount of new blood vessels formed. High-magnification images of histology sections were used to identify vessels at the center and the edges of these wounds (Figure 5g). In agreement with the granulation tissue-formation data, these images confirmed formation of dense networks of blood vessels at these select wound areas and were measured in higher numbers for the HA-treatment groups when compared to controls (Figure 5h). Together, these data confirm the ability of HA fiber scaffold to support necessary tissue-repair processes in a cutaneous wound-healing context.

DISCUSSION

Designing organ-specific proregenerative materials requires the ability to precisely tune biophysical and biochemical properties to support and stimulate an endogenous response.[6−8] In this context, the versatility of a nanofiber manufacturing method—termed immersed rotary jet spinning (iRJS)[45]—was investigated for engineering tunable hyaluronic acid scaffolds, while achieving similar fabrication flexibility with a wide range of other ECM molecules. Either in pure form or as hybrids, these engineered materials formed fibrous scaffolds at production rates readily amenable to clinical translation, while being fashioned from entirely aqueous solutions. Overcoming the need to rely on organic solvents may prove advantageous as these chemicals have been shown to denature ECM proteins and effectively reduce their biological functionality.[32,66] Synthetic polymers or hydrogels, such as polyethylene glycol, could likely be processed using this system, while other materials, such as alginate or DNA, were already tested[45] but are beyond the scope of this study. The high-throughput manufacturing capabilities furthermore spurred the establishment of a comprehensive structural and mechanical parameter framework, achievable within an iRJS system. Notably, we observed that fiber diameters could range from hundreds of nanometers to several microns, while high porosity, water absorbency, and tissue-level mechanics were inherent features of all HA-based fiber scaffolds. This parameter space offers in theory biomimetic properties for a range of different tissues (for example, skin, adipose tissue, or brain) or specific biological responses.[7] Degradation kinetics and porosity could furthermore be tuned, thus offering a holistic approach for designing the structural and mechanical properties of proregenerative materials.

When compared to clinically available HA skin substitutes,[67] our method enabled fabrication of smaller fibers by an order of magnitude—a size scale (~1um) that may facilitate interaction with cells, and therefore prove advantageous for cell migration, proliferation, and scaffold remodeling.[26,68] Conversely, spinning methods focused on the development of low-micron and submicron HA fibers, while successful, may have suffered from low scaffold porosities and poor production capabilities (such as heterogeneous scaffold structure),[42,43,56] thus impeding their preclinical investigation and subsequent translation to the clinic. Our manufacturing approach may offer a new avenue for exploring fiber-based HA medical products.

DOI: 10.1021/acsami.9b17322
ACS Appl. Mater. Interfaces XXXX, XXX, XXX−XXX

In this study, HA scaffolds, composed of fibers of ∼1 μm, were collected into large centimeter-wide sheets and cut into 500-μm-thick circular dressings for studies in vitro and applications in an excisional splinting wound mouse model in vivo. We first sought to understand the effect of highly porous scaffolds (pHA, ∼95%) on cellular infiltration. Porosity indeed remains a critical regulator in supporting rapid scaffold integration, which subsequently facilitates downstream tissue-repair mechanisms.[39] In vitro, we measured rapid and in-depth permeation of seeded dermal fibroblasts, with a roughly homogeneous distribution, while biocompatibility and bioactivity were observed up to 7 days in culture. By contrast, the denser mHA and dHA scaffolds (of ∼85% and ∼70% porosity, respectively)—while remaining porous in comparison to other nanofiber scaffolds[47]—demonstrated stronger accumulation of cells at the scaffold's surface and concomitant poorer ingress. Moving forward, the ability of cells to form cell-adhesion complexes and proliferate in these scaffolds could likely be improved through the incorporation of adhesion molecules or peptides.

When investigating these scaffolds in a wound mouse model, data first revealed that both pHA and mHA scaffolds supported the wound-closure process, contributing to the rapid formation of scabs and new tissues over the wounds. Histological analysis then underscored the relevance of higher porosity, exemplified by the rapid formation of granulation tissues, neovascularization, and long protruding epithelial tongues 6 days after injury in the pHA specimen. The mHA dressing initiated tissue repair, yet at a lower level, illustrated by the larger gaps remaining between the wound edges and less granulation tissue formation. These observations corroborate previous studies of nanofiber scaffolds for tissue-engineering applications, where insufficient porosity was detrimental to scaffold integration within host tissues, thus leading to poorer remodeling.[39,40]

Altogether, these data reveal how designing materials with faithful biomimetic features, such as mechanical and structural properties, and that are amenable to rapid tissue integration through a porous interface can potentiate tissue repair. The influence of porosity, highlighted in vitro and in vivo, was in particular made evident by the poor cellular ingress and slower tissue formation in denser scaffolds. Nonetheless, all HA scaffolds demonstrated influence within the first week of treatment, embodied by faster scab formation, reepithelialization, neovascularization, and granulation tissue formation, which is particularly relevant in the context of difficult-to-heal wounds.[4,5] Moving forward, acting as an instructive backbone integrated with additional functional groups, these biomimetic porous HA scaffolds may be able to achieve stronger functionality in vitro and more robust tissue repair and regeneration in vivo.

CONCLUSION

In this study, we manufactured a variety of porous biomimetic nanofiber scaffolds from ECM molecules including hyaluronic acid, fibrinogen, collagen, gelatin, and chondroitin sulfate using an iRJS system. The high-throughput nature of the system, as well as its flexible spinning conditions and postprocessing modifications, were leveraged here to investigate the manufacturing parameter space of hyaluronic acid fiber scaffolds. Nano- to micrometer fiber diameters, highly porous, water-absorbent, and soft-tissue mimetic mechanical properties were attainable with this system. By controlling interfiber bonding, the porosity of HA scaffolds could be tuned from 70 to 95%, enabling identification of high porosity as an important mediator for in-depth cellular ingress in vitro. Porous HA scaffolds (85% and 95% porosity) were tested in an excisional splinted wound healing model in mice and demonstrated the ability to support faster wound closure, reepithelialization, granulation tissue formation, and neovascularization within the first week of treatment. The in vitro and in vivo data further reaffirmed the influence that scaffold properties, such as porosity, can have on wound healing and reparative processes. Altogether, this study demonstrated the fabrication of tunable ECM-based nanofiber scaffolds that may arise as potent building blocks for designing more comprehensive proregenerative solutions.

MATERIALS AND METHODS

Design of Production-Scale iRJS System. The iRJS system consists of six main components: (1) a custom-machined 7075 aluminum reservoir coated with AMS 2482 Type 1 anodized hard coat, Teflon with 1 mil build up (25 um), an inner diameter of 40 mm, and two cylindrical orifices of 300 μm; (2) a remote-controlled electric motor with rotation speeds ranging from 1 000 to 80 000 rpm; (3) a custom-built chemical resistant epoxy-coated cylindrical polycarbonate precipitation bath container with an inner diameter of 28 cm and a working volume of ∼5 L; (4) a custom-built aluminum rotating vortex generator connected via rotary sealed shaft to a pulley driven by motor with a spinning range of 1−500 rpm; (5) 3D-printed cylindrical sample collectors of variable diameters (from 8 to 20 cm) and height (from 5 to 20 cm), for tailored fiber sheet sizes; and (6) a remote-controlled syringe pump (PHD Ultra, Harvard Apparatus), providing working extrusion rates of 0.1−20 mL/min. The iRJS system was further placed in a humidity-controlled chamber.

Protein Solution Preparation and Spinning. All ECM molecules (obtained from Sigma) described in this study were dissolved in aqueous solutions and spun into solvent-miscible precipitation baths, thus enabling rapid solvent dissolution and precipitation of the ECM molecule into fibrous structures. Briefly, specific ECM molecule solution preparation and spinning methods are described.

Hyaluronic Acid. Hyaluronic acid (HA) was purchased (hyaluronic acid sodium salt from Streptococcus equi, ∼1500−1800 kDa MW, Sigma) as a powder and dissolved in diH_2O and NaCl at various concentrations (from 1−4% weight/volume (w/v) and 0−600 mM, respectively) for 24−48 h at room temperature. See Table S1 for details. A precipitation bath of 80% ethanol was used.

Chondroitin Sulfate. Chondroitin sulfate (CS) was purchased (chondroitin sulfate sodium salt from shark cartilage, Sigma) as a powder and dissolved at 20% w/v in diH_2O for 24−48 h at room temperature. See Table S1 for details. A precipitation bath of 80% ethanol was used.

Collagen Type I. Collagen type I (ColI) was purchased (solution from rat tail, Sigma) in an aqueous solution of 20 mM acetic acid at a concentration of ∼4−4.5% w/v. ColI was either spun directly from the purchased solution or purified through dialysis for 24 h in 10% poly(ethylene glycol) (PEG) to reach a final concentration of ∼10% w/v. A precipitation bath of 80% ethanol was used.

Gelatin. Gelatin (Gel) was purchased (bovine tendon, Bloom 300, Sigma) as a powder and dissolved at various concentrations in diH_2O (see Table S1) at 37 °C for 24 h. Because concentrated Gel solutions form solid-like gels at RT, dope solutions were kept at or above 30 °C, thus maintaining low enough viscosity to allow extrusion in the rotating reservoir of the iRJS. A bath of 95% ethanol was used to precipitate Gel fibers.

Fibrinogen. Fibrinogen (Fb) was purchased (bovine plasma, Type I−S, Sigma) as a powder and dissolved at various concentrations (see Table S1) in Dulbecco's modified Eagle medium (DMEM) (Thermofisher) at 37 °C for 3−4 days. Fb solution was then brought to room temperature (RT) and spun in a bath of 95% ethanol.

All solution dopes were loaded into a syringe and extruded in the iRJS rotating reservoir. Fibers were then collected in the precipitation

DOI: 10.1021/acsami.9b17322
ACS Appl. Mater. Interfaces XXXX, XXX, XXX−XXX

bath. Different speeds were used for different protein solutions (see Table S1 for detailed specifications). Unless otherwise specified, air-gap distance was set at ∼5 cm. After spinning, fiber samples were briefly stored in their respective precipitation baths at −80 °C and subsequently lyophilized before use.

Scaffold Rehydration, Lyophilization, and Cross-linking. To increase density of HA nanofiber scaffolds, rehydration was performed by removing the sample from the precipitation bath and positioning it horizontally in a Petri dish. Sample sizes were kept identical when rehydration was performed. Rehydration times of 0−60 min were used. Alternatively, samples were directly placed in a −80 °C freezer and subsequently lyophilized. If cross-linked, samples were placed in a solution of 80% ethanol with 10 mM EDC and 4 mM NHS for 24 h on a shaker. Samples were then washed several times in diH_2O and DMEM, before lyophilizing again and storing at 4 °C.

Scanning Electron Micrography and Characterization of Fiber Size. Fiber samples were mounted on scanning electron micrograph (SEM) stubs and coated with 5−20 nm of platinum/palladium (Pt/Pd) using an EMS 300T Sputter Coater (Quorum Technologies) to minimize charge accumulation during imaging. Thin samples were coated with 5 nm of Pt/Pd, while thick and porous samples were coated with up to 20 nm. SEM imaging was then performed using a field-emitting SEM (FESEM Ultra55, Zeiss) at a voltage of 5 kV. For fiber diameter and porosity measurements, 6−8 fields of view at 1 000× or 2 000× magnification (depending on fiber size) were made per sample. Three different sample runs at least were used. Measurements were performed using the FIJI analysis software (ImageJ, NIH): fiber diameter was measured using the linear measuring tool, whereas porosity was calculated using the percentage tool (fiber vs nonfiber) on SEM binary images.

Porosity Measurements. Scaffold porosity was measured using an established liquid-displacement method used for tissue-engineering scaffolds.[69] Briefly, the scaffolds are submerged in a graduated cylinder with a liquid of a known volume (V_1), thereby increasing the volume to a new value (liquid + scaffold = V_2). Ethanol was used here as the liquid, being a precipitant of HA, to penetrate the scaffolds without shrinking or swelling them. The ethanol-impregnated scaffolds were then removed, and the liquid displaced was measured (V_3), after which a porosity value could be calculated using the following equation: porosity = $(V_1 - V_3)/(V_2 - V_3)$.

Rheology Measurements. Rheology studies were conducted to measure viscosity profiles of HA solutions of different concentrations (1−4% w/v). Briefly, rheological properties were determined using a TA Instruments Discovery Hybrid 3 Rheometer with a cone plate geometry. The cone had a 40 mm diameter, 1° angle, and 26 μm truncation gap. The plate was temperature-controlled to 25 °C, and a solvent trap was used to ensure the sample did not lose solvent during testing. All materials in contact with the sample were aluminum. To load the sample, the cone was brought to a height above the plate defined by the truncation gap. After trimming the sample, the cone was raised and then brought back to the truncation gap. This repetition was employed to reduce normal forces generated during loading. After loading, a 300 s soak time ensured that the sample reached equilibrium. The solution was sampled at a rate of 10 points per decade over 10^{-3} to 10^{4} (1/s). To ensure the solution reached equilibrium during each of these samplings, steady-state sensing was used over 180 s of testing. If subsequent 30 s sample periods were with 5% tolerance of one another, then the sample was determined to have reached steady state and the next point was sampled. Testing revealed that, below 10^{-1} (1/s) shear rates, the solution-rheometer system was dominated by surface forces, while above 10^{-4} (1/s) shear rates, the system was dominated by momentum. As these shear rates were not dominated by viscous force, they were not included in the data presented.

X-ray Micro Computed Tomography. X-ray micro computed tomography (μCT) was performed with an X-Tek HMXST225 system (Nikon Metrology, Inc.) equipped with a 225 kV microfocus X-ray source with 3 μm focal spot size. Fiber samples were incubated for 24 h on a shaker in a 1:10 dilution of Lugols's iodine solution to improve contrast upon imaging. An aluminum target and 115 kV accelerating voltage were used. Image acquisition and reconstruction were performed with InspectX (X-ray imaging and CT acquisition), CT Pro 3D (volume reconstruction), and VG Studio MAX 2.2 (3D volume visualization, rendering, and analysis).

Fourier Transform Infrared Spectroscopy. Attenuated total reflection Fourier transform infrared spectroscopy (ATR-FTIR) (Bruker) was performed to obtain infrared spectra of HA nanofibers and raw lyophilized powder over 600−4000 cm^{-1} at a resolution of 2 cm^{-1} with 16 scans. Measurements were normalized from 0 to 1. Graph plotting and analysis were performed using OriginPro 8.6 software (Origin Lab Corporation). For statistical analysis, at least 3 different areas were measured on each sample.

Swelling Ratio and Degradation Kinetics. Lyophilized HA nanofiber samples were cut into ∼5 mg samples. Water absorption was calculated using the swelling ratio commonly used for hydrogels. The swelling ratio (SR) is defined as SR = $(W_h - W_d)/W_d$, where W_d is the weight of dry sample and W_h is the weight of hydrated sample. Nanofiber samples were hydrated in diH_2O for 5 min before measurements. Degradation was evaluated by measuring loss in weight of hydrated samples in diH_2O over time (up to 10 000 min (∼1 week)).

Mechanical Testing. Mechanical properties were measured in extension using a CellScale biaxial tensile tester (0.5 N load cells, Biotester, CellScale) and in compression using an Instron universal testing machine (model 5566, Instron). Briefly, for tensile testing, samples were cut in rectangular shapes (5 × 10 mm) with a thickness of 2 mm, hydrated with phosphate-buffered saline (PBS), mounted for uniaxial testing, and tested using a 50% strain at 10% strain rate. Strain was applied parallel to fiber orientation. Measurements were performed at 37 °C in PBS. Mechanical testing in compression was performed with square samples (5 × 5 mm) with a thickness of 2 mm. Strain was set at 40% with 10% strain rate. Measurements were performed at RT in PBS. For both testing experiments, stress−strain curves were calculated for each sample and modulus was extracted.

In Vitro Cell Permeation, Biocompatibility, and Bioactivity Studies. GFP-expressing human dermal neonatal fibroblasts (GFP-HNDFs, Angioproteomie) were seeded on fiber HA fiber scaffolds (100 000 cells per sample) and imaged 30 min later using a confocal microscope (Olympus) under controlled culture conditions (37 °C and 95% humidity). Z-stack images were taken from the scaffolds surface to depths exceeding 100 μm. Image analysis, 3D reconstruction renderings, and permeation intensity values were performed and quantified using FIJI analysis software. Alternatively, fibroblasts were cultured for 24 h and up to 7 days and subsequently fixed and permeabilized with paraformaldehyde (PFA) and Triton-X, respectively, before being immunostained with DAPI (nuclei) and Phalloidin (F-actin) for 2 h at dilutions of 1:200 and imaged under confocal microscope. GFP-HNDFs were cultured in cell growth medium consisting of Dulbecco's modified eagle medium (DMEM, ThermoFisher Scientific), 5% fetal bovine serum, and 1% antibiotics (penicillin-streptomycin, ThermoFisher Scientific). Passages were made before cells reached 80% confluency and used for experiments until passage number 15.

Cytotoxicity Measurements. The cytotoxicity of HA fiber scaffolds was tested using a commercial lactic acid dehydrogenase (LDH) assay (Promega, U.S.A.). Cell culture media were collected at 7 days of cell culture from both HA scaffolds and nonfiber controls and incubated with the reagents for 30 min at room temperature. The stop solutions were then added to the samples and absorbance was measured at 490 nm using a microplate reader to measure LDH levels (BioTek, U.S.A.).

In Vivo Wound Healing Studies. All animal studies were performed following approved procedures by the Harvard University Institutional Animal Care and Use Committee (IACUC). The protocol follows the previously established excisional wound splinting model that enables wound closure by reepithelialization instead of by wound contraction.[65] Briefly, C57BL/6 male mice (8−10 weeks old) (Charles River Laboratories, Wilmington, MA) were anesthetized and maintained on surgical plane of anesthesia with isoflurane. After a toe pinch test was performed to confirm anesthesia, the backs of the mice were first prepared by shaving with an electric razor (Kent Scientific, BravMini Pro, CL7300). The surgical area was then sterilized with

DOI: 10.1021/acsami.9b17322
ACS Appl. Mater. Interfaces XXXX, XXX, XXX−XXX

alcohol and betadine (at least 2× each). A line across the centerline of the back was made with a surgical marker to facilitate positioning. Two full-thickness wounds were made on the back, lateral to the spin on both sides using 6 mm biopsy punches. Silicon splinting rings (o.d., 10 mm; i.d., 6 mm), sterilized in ethanol and under UV overnight, were applied and set in place with instant-bonding adhesive glue and sutured with 4 surgical knots. Nanofiber HA wound dressings were prepared in large sheets (20 × 10 × 1 mm), cut out into 6 mm wide discs (1 mm thick) using a biopsy punch, sterilized overnight under UV, applied to the wound with 5 μL of PBS to facilitate adherence, and covered with Tegaderm silicon patches. Mice were monitored daily. Photographic images of the wounds were performed every 3 days. Tissues were collected on day 6 to assess granulation tissue formation, reepithelialization, and scaffold integration, whereas long-term tracking was performed up to day 28. Treatments and control application was randomized.

Histology Analysis. Histology was performed by HMS Rodent Histopathology Core following standard protocols. Tissues were harvested at days 6 and 28 after wounding and fixed with 4% paraformaldehyde for 15 min. For day 6 analysis, samples were then washed and stored in PBS before PFA embedding, sectioning, and staining. Whole-slide imaging was performed using a slide scanner (Virtual Slide Microscope VS120, Olympus) with a 20× objective. Granulation tissue formation and reepithelialization were analyzed using FIJI image analysis software. High-magnification fields of view (FOVs) of 540 μm × 300 μm and figure display images (270 μm × 150 μm) of blood vessels were generated and analyzed using OlyVIA software (Olympus).

Statistical Analysis. Statistical analyses were conducted using SigmaPlot (v12.0, Systat Software, Inc., CA). One-way ANOVA on ranks with post hoc multiple comparisons Dunn's test, Holm−Sidak's test, or Student's *t* test were used where appropriate. Quantitative data are presented as mean ± s.e.m., and significance was considered for $p < 0.05$.

■ ASSOCIATED CONTENT

Supporting Information

The Supporting Information is available free of charge at https://pubs.acs.org/doi/10.1021/acsami.9b17322.

HA fabrication process of internally aligned fiber-based scaffolds; versatile material fabrication capabilities; ECM materials spinning parameters; rheological measurements of HA dopes; SEM images of sectioned HA nanofiber scaffolds; rotation speed-dependent fiber diameters; representative SEMs of varying scaffold porosities produced by nanofiber spinning platforms; water absorption and degradation of HA scaffolds; fiber diameter and porosity of as-spun and cross-linked; cytocompatibility of HA scaffolds using LDH assay; long-term wound-closure monitoring; additional control histological sections; additional mHA histological sections; and additional pHA histological sections (PDF)

Rapid manufacture and collection of HA nanofibers using the iRJS system, with fibers becoming gradually visible as a white sheet and being wrapped around a blue collector (time × 8) (MP4)

Stability of a cross-linked HA nanofiber scaffold when submerged in water; scaffold colored with a food dye (red) for improved clarity (MP4)

High elastic nature and hydrophilicity of HA fibers as they stretch; recovery and recoil as they rehydrate (time × 2) (MP4)

High elastic nature and hydrophilicity of HA fibers as they stretch; recovery and recoil as they rehydrate (MP4)

■ AUTHOR INFORMATION

Corresponding Author

*Tel.: (617) 495-2850. Fax: (617) 495-9837. E-mail: kkparker@seas.harvard.edu.

ORCID

Kevin Kit Parker: 0000-0002-5968-7535

Author Contributions

C.O.C. and K.K.P. designed the study. G.M.G. designed the manufacturing platform. C.O.C., G.M.G., S.A., L.C., P.H.C., S.P.H., and K.K.P. supported with data collection, analysis, and interpretation. C.O.C. and K.K.P. wrote the manuscript.

Notes

The authors declare no competing financial interest.

■ ACKNOWLEDGMENTS

The authors thank the Wyss Institute of Biologically Inspired Engineering at Harvard University and the Institute for Regenerative Medicine (IREM) at University of Zurich for their ongoing support throughout this project. The authors also thank Luke MacQueen for his helpful advice and comments on manuscript, Gabriela Berner and Thomas Grevesse for their initial support with developing and characterizing HA scaffolds, and Michael Rosnach for his support with photography and illustrations. This project was also in part conducted at Harvard Center for Nanoscale Systems (CNS), which is a member of the National Nanotechnology Infrastructure Network (NNIN), supported by the National Science Foundation under NSF Award no. 1541959. CNS is part of Harvard University. The authors thank Greg Lin from CNS for his support with μCT tests. We also thank the Harvard Medical School Department of Neurobiology Imaging Facility for consultation and instrumentation availability that supported this work. The Neurobiology Imaging Facility is supported in part by the Neural Imaging Center as part of a NINDS P30 Core Center Grant no. NS072030. We thank the Dana-Farber/Harvard Cancer Center in Boston for the use of the Rodent Histopathology Core, which provided sample-preparation service. Dana-Farber/Harvard Cancer Center is supported in part by a NCI Cancer Center Support Grant no. NIH 5 P30 CA06516. This work was also funded in part by the Harvard Materials Research Science and Engineering Center (DMR-14-20570). The content is solely the responsibility of the authors and does not necessarily represent the official views of the funding agencies and institutions.

■ REFERENCES

(1) Sen, C. K.; Gordillo, G. M.; Roy, S.; Kirsner, R.; Lambert, L.; Hunt, T. K.; Gottrup, F.; Gurtner, G. C.; Longaker, M. T. Human skin wounds: a major and snowballing threat to public health and the economy. *Wound repair and regeneration: official publication of the Wound Healing Society [and] the European Tissue Repair Society* **2009**, *17* (6), 763−71.

(2) Singer, A. J.; Clark, R. A. Cutaneous wound healing. *N. Engl. J. Med.* **1999**, *341* (10), 738−46.

(3) Gurtner, G. C.; Werner, S.; Barrandon, Y.; Longaker, M. T. Wound repair and regeneration. *Nature* **2008**, *453* (7193), 314−21.

(4) Haddad, A. G.; Giatsidis, G.; Orgill, D. P.; Halvorson, E. G. Skin Substitutes and Bioscaffolds: Temporary and Permanent Coverage. *Clinics in plastic surgery* **2017**, *44* (3), 627−634.

(5) Frykberg, R. G.; Banks, J. Challenges in the Treatment of Chronic Wounds. *Advances in wound care* **2015**, *4* (9), 560−582.

(6) Lutolf, M. P.; Hubbell, J. A. Synthetic biomaterials as instructive extracellular microenvironments for morphogenesis in tissue engineering. *Nat. Biotechnol.* **2005**, *23* (1), 47−55.

DOI: 10.1021/acsami.9b17322
ACS Appl. Mater. Interfaces XXXX, XXX, XXX−XXX

(7) Chantre, C. O.; Hoerstrup, S. P.; Parker, K. K. Engineering biomimetic and instructive materials for wound healing and regeneration. *Current Opinion in Biomedical Engineering* **2019**, *10*, 97−106.
(8) Rice, J. J.; Martino, M. M.; De Laporte, L.; Tortelli, F.; Briquez, P. S.; Hubbell, J. A. Engineering the regenerative microenvironment with biomaterials. *Adv. Healthcare Mater.* **2013**, *2* (1), 57−71.
(9) Moore, A. L.; Marshall, C. D.; Barnes, L. A.; Murphy, M. P.; Ransom, R. C.; Longaker, M. T. Scarless wound healing: Transitioning from fetal research to regenerative healing. *WIREs Dev. Biol.* **2018**, *7* (2), e309.
(10) Pashuck, E. T.; Stevens, M. M. Designing regenerative biomaterial therapies for the clinic. *Sci. Transl. Med.* **2012**, *4* (160), 160sr4.
(11) Hynes, R. O. The extracellular matrix: not just pretty fibrils. *Science (Washington, DC, U. S.)* **2009**, *326* (5957), 1216−9.
(12) Frantz, C.; Stewart, K. M.; Weaver, V. M. The extracellular matrix at a glance. *J. Cell Sci.* **2010**, *123* (24), 4195−200.
(13) Dicker, K. T.; Gurski, L. A.; Pradhan-Bhatt, S.; Witt, R. L.; Farach-Carson, M. C.; Jia, X. Hyaluronan: a simple polysaccharide with diverse biological functions. *Acta Biomater.* **2014**, *10* (4), 1558−70.
(14) Iocono, J. A.; Ehrlich, H. P.; Keefer, K. A.; Krummel, T. M. Hyaluronan induces scarless repair in mouse limb organ culture. *Journal of pediatric surgery* **1998**, *33* (4), 564−7.
(15) Ouyang, X.; Panetta, N. J.; Talbott, M. D.; Payumo, A. Y.; Halluin, C.; Longaker, M. T.; Chen, J. K. Hyaluronic acid synthesis is required for zebrafish tail fin regeneration. *PLoS One* **2017**, *12* (2), e0171898.
(16) Calve, S.; Odelberg, S. J.; Simon, H. G. A Transitional Extracellular Matrix Instructs Cell Behavior During Muscle Regeneration. *Dev. Biol.* **2010**, *344* (1), 259−71.
(17) Longaker, M. T.; Adzick, N. S.; Hall, J. L.; Stair, S. E.; Crombleholme, T. M.; Duncan, B. W.; Bradley, S. M.; Harrison, M. R.; Stern, R. Studies in fetal wound healing, VII. Fetal wound healing may be modulated by hyaluronic acid stimulating activity in amniotic fluid. *Journal of pediatric surgery* **1990**, *25* (4), 430−433.
(18) Highley, C. B.; Prestwich, G. D.; Burdick, J. A. Recent advances in hyaluronic acid hydrogels for biomedical applications. *Curr. Opin. Biotechnol.* **2016**, *40*, 35−40.
(19) Jha, A. K.; Tharp, K. M.; Ye, J.; Santiago-Ortiz, J. L.; Jackson, W. M.; Stahl, A.; Schaffer, D. V.; Yeghiazarians, Y.; Healy, K. E. Enhanced survival and engraftment of transplanted stem cells using growth factor sequestering hydrogels. *Biomaterials* **2015**, *47*, 1−12.
(20) Purcell, B. P.; Lobb, D.; Charati, M. B.; Dorsey, S. M.; Wade, R. J.; Zellars, K. N.; Doviak, H.; Pettaway, S.; Logdon, C. B.; Shuman, J. A.; Freels, P. D.; Gorman, J. H., 3rd; Gorman, R. C.; Spinale, F. G.; Burdick, J. A. Injectable and bioresponsive hydrogels for on-demand matrix metalloproteinase inhibition. *Nat. Mater.* **2014**, *13* (6), 653−61.
(21) Bian, L.; Guvendiren, M.; Mauck, R. L.; Burdick, J. A. Hydrogels that mimic developmentally relevant matrix and N-cadherin interactions enhance MSC chondrogenesis. *Proc. Natl. Acad. Sci. U. S. A.* **2013**, *110* (25), 10117−22.
(22) Tokatlian, T.; Cam, C.; Segura, T. Porous hyaluronic acid hydrogels for localized nonviral DNA delivery in a diabetic wound healing model. *Adv. Healthcare Mater.* **2015**, *4* (7), 1084−91.
(23) Tokatlian, T.; Cam, C.; Segura, T. Non-viral DNA delivery from porous hyaluronic acid hydrogels in mice. *Biomaterials* **2014**, *35* (2), 825−35.
(24) Motolese, A.; Vignati, F.; Brambilla, R.; Cerati, M.; Passi, A. Interaction between a regenerative matrix and wound bed in nonhealing ulcers: results with 16 cases. *BioMed Res. Int.* **2013**, *2013*, 849321.
(25) Gjorevski, N.; Sachs, N.; Manfrin, A.; Giger, S.; Bragina, M. E.; Ordonez-Moran, P.; Clevers, H.; Lutolf, M. P. Designer matrices for intestinal stem cell and organoid culture. *Nature* **2016**, *539* (7630), 560−564.
(26) Wang, X.; Ding, B.; Li, B. Biomimetic electrospun nanofibrous structures for tissue engineering. *Mater. Today* **2013**, *16* (6), 229−241.
(27) Ahn, S.; Chantre, C. O.; Gannon, A. R.; Lind, J. U.; Campbell, P. H.; Grevesse, T.; O'Connor, B. B.; Parker, K. K. Soy Protein/Cellulose Nanofiber Scaffolds Mimicking Skin Extracellular Matrix for Enhanced Wound Healing. *Adv. Healthcare Mater.* **2018**, *7* (9), 1701175.
(28) Chantre, C. O.; Campbell, P. H.; Golecki, H. M.; Buganza, A. T.; Capulli, A. K.; Deravi, L. F.; Dauth, S.; Sheehy, S. P.; Paten, J. A.; Gledhill, K.; Doucet, Y. S.; Abaci, H. E.; Ahn, S.; Pope, B. D.; Ruberti, J. W.; Hoerstrup, S. P.; Christiano, A. M.; Parker, K. K. Production-scale fibronectin nanofibers promote wound closure and tissue repair in a dermal mouse model. *Biomaterials* **2018**, *166*, 96−108.
(29) Zhu, M.; Wu, Y.; Li, W.; Dong, X.; Chang, H.; Wang, K.; Wu, P.; Zhang, J.; Fan, G.; Wang, L.; Liu, J.; Wang, H.; Kong, D. Biodegradable and elastomeric vascular grafts enable vascular remodeling. *Biomaterials* **2018**, *183*, 306−318.
(30) Reneker, D. H.; Yarin, A. L. Electrospinning jets and polymer nanofibers. *Polymer* **2008**, *49* (10), 2387−2425.
(31) Puppi, D.; Chiellini, F. Wet-spinning of biomedical polymers: from single-fibre production to additive manufacturing of three-dimensional scaffolds. *Polym. Int.* **2017**, *66* (12), 1690−1696.
(32) Zeugolis, D. I.; Khew, S. T.; Yew, E. S.; Ekaputra, A. K.; Tong, Y. W.; Yung, L. Y.; Hutmacher, D. W.; Sheppard, C.; Raghunath, M. Electro-spinning of pure collagen nano-fibres - just an expensive way to make gelatin? *Biomaterials* **2008**, *29* (15), 2293−305.
(33) Webber, M. J.; Khan, O. F.; Sydlik, S. A.; Tang, B. C.; Langer, R. A perspective on the clinical translation of scaffolds for tissue engineering. *Ann. Biomed. Eng.* **2015**, *43* (3), 641−56.
(34) Capulli, A. K.; MacQueen, L. A.; Sheehy, S. P.; Parker, K. K. Fibrous scaffolds for building hearts and heart parts. *Adv. Drug Delivery Rev.* **2016**, *96*, 83−102.
(35) Pham, Q. P.; Sharma, U.; Mikos, A. G. Electrospun poly(epsilon-caprolactone) microfiber and multilayer nanofiber/microfiber scaffolds: characterization of scaffolds and measurement of cellular infiltration. *Biomacromolecules* **2006**, *7* (10), 2796−805.
(36) Telemeco, T. A.; Ayres, C.; Bowlin, G. L.; Wnek, G. E.; Boland, E. D.; Cohen, N.; Baumgarten, C. M.; Mathews, J.; Simpson, D. G. Regulation of cellular infiltration into tissue engineering scaffolds composed of submicron diameter fibrils produced by electrospinning. *Acta Biomater.* **2005**, *1* (4), 377−85.
(37) Novosel, E. C.; Kleinhans, C.; Kluger, P. J. Vascularization is the key challenge in tissue engineering. *Adv. Drug Delivery Rev.* **2011**, *63* (4−5), 300−11.
(38) Wade, R. J.; Bassin, E. J.; Rodell, C. B.; Burdick, J. A. Protease-degradable electrospun fibrous hydrogels. *Nat. Commun.* **2015**, *6*, 6639.
(39) Baker, B. M.; Shah, R. P.; Silverstein, A. M.; Esterhai, J. L.; Burdick, J. A.; Mauck, R. L. Sacrificial nanofibrous composites provide instruction without impediment and enable functional tissue formation. *Proc. Natl. Acad. Sci. U. S. A.* **2012**, *109* (35), 14176−81.
(40) Jiang, J.; Li, Z.; Wang, H.; Wang, Y.; Carlson, M. A.; Teusink, M. J.; MacEwan, M. R.; Gu, L.; Xie, J. Expanded 3D Nanofiber Scaffolds: Cell Penetration, Neovascularization, and Host Response. *Adv. Healthcare Mater.* **2016**, *5* (23), 2993−3003.
(41) Li, J.; He, A.; Zheng, J.; Han, C. C. Gelatin and gelatin-hyaluronic acid nanofibrous membranes produced by electrospinning of their aqueous solutions. *Biomacromolecules* **2006**, *7* (7), 2243−7.
(42) Li, J.; He, A.; Han, C. C.; Fang, D.; Hsiao, B. S.; Chu, B. Electrospinning of Hyaluronic Acid (HA) and HA/Gelatin Blends. *Macromol. Rapid Commun.* **2006**, *27* (2), 114−120.
(43) Um, I. C.; Fang, D.; Hsiao, B. S.; Okamoto, A.; Chu, B. Electro-spinning and electro-blowing of hyaluronic acid. *Biomacromolecules* **2004**, *5* (4), 1428−36.
(44) Lee, K. Y.; Jeong, L.; Kang, Y. O.; Lee, S. J.; Park, W. H. Electrospinning of polysaccharides for regenerative medicine. *Adv. Drug Delivery Rev.* **2009**, *61* (12), 1020−32.
(45) Gonzalez, G. M.; MacQueen, L. A.; Lind, J. U.; Fitzgibbons, S. A.; Chantre, C. O.; Huggler, I.; Golecki, H. M.; Goss, J. A.; Parker, K. K. Production of Synthetic, Para-Aramid and Biopolymer Nanofibers by Immersion Rotary Jet-Spinning. *Macromol. Mater. Eng.* **2017**, *302* (1), 1600365.

DOI: 10.1021/acsami.9b17322
ACS Appl. Mater. Interfaces XXXX, XXX, XXX−XXX

(46) Badrossamay, M. R.; McIlwee, H. A.; Goss, J. A.; Parker, K. K. Nanofiber assembly by rotary jet-spinning. *Nano Lett.* **2010**, *10* (6), 2257−61.
(47) Capulli, A. K.; Emmert, M. Y.; Pasqualini, F. S.; Kehl, D.; Caliskan, E.; Lind, J. U.; Sheehy, S. P.; Park, S. J.; Ahn, S.; Weber, B.; Goss, J. A.; Hoerstrup, S. P.; Parker, K. K. JetValve: Rapid manufacturing of biohybrid scaffolds for biomimetic heart valve replacement. *Biomaterials* **2017**, *133*, 229−241.
(48) MacQueen, L. A.; Alver, C. G.; Chantre, C. O.; Ahn, S.; Cera, L.; Gonzalez, G. M.; O'Connor, B. B.; Drennan, D. J.; Peters, M. M.; Motta, S. E.; Zimmerman, J. F.; Parker, K. K. Muscle tissue engineering in fibrous gelatin: implications for meat analogs. *npj Sci. Food* **2019**, *3* (1), 20.
(49) Kim, I. L.; Khetan, S.; Baker, B. M.; Chen, C. S.; Burdick, J. A. Fibrous hyaluronic acid hydrogels that direct MSC chondrogenesis through mechanical and adhesive cues. *Biomaterials* **2013**, *34* (22), 5571−80.
(50) Badrossamay, M. R.; Balachandran, K.; Capulli, A. K.; Golecki, H. M.; Agarwal, A.; Goss, J. A.; Kim, H.; Shin, K.; Parker, K. K. Engineering hybrid polymer-protein super-aligned nanofibers via rotary jet spinning. *Biomaterials* **2014**, *35* (10), 3188−97.
(51) Mellado, P.; McIlwee, H. A.; Badrossamay, M. R.; Goss, J. A.; Mahadevan, L.; Parker, K. K. A simple model for nanofiber formation by rotary jet-spinning. *Appl. Phys. Lett.* **2011**, *99* (20), 203107.
(52) MacQueen, L. A.; Sheehy, S. P.; Chantre, C. O.; Zimmerman, J. F.; Pasqualini, F. S.; Liu, X.; Goss, J. A.; Campbell, P. H.; Gonzalez, G. M.; Park, S.-J.; Capulli, A. K.; Ferrier, J. P.; Kosar, T. F.; Mahadevan, L.; Pu, W. T.; Parker, K. K. A tissue-engineered scale model of the heart ventricle. *Nature Biomedical Engineering* **2018**, *2* (12), 930−941.
(53) Deravi, L. F.; Golecki, H. M.; Parker, K. K. Protein-Based Textiles: Bio-Inspired and Bio-Derived Materials for Medical and Non-Medical Applications. *Journal of Chemical and Biological Interfaces* **2013**, *1* (1), 25−34.
(54) Xia, H.; Li, X.; Gao, W.; Fu, X.; Fang, R. H.; Zhang, L.; Zhang, K. Tissue repair and regeneration with endogenous stem cells. *Nature Reviews Materials* **2018**, *3* (7), 174−193.
(55) Persano, L.; Camposeo, A.; Tekmen, C.; Pisignano, D. Industrial Upscaling of Electrospinning and Applications of Polymer Nanofibers: A Review. *Macromol. Mater. Eng.* **2013**, *298* (5), 504−520.
(56) Uppal, R.; Ramaswamy, G. N.; Arnold, C.; Goodband, R.; Wang, Y. Hyaluronic acid nanofiber wound dressing–production, characterization, and in vivo behavior. *J. Biomed. Mater. Res., Part B* **2011**, *97* (1), 20−9.
(57) Nezarati, R. M.; Eifert, M. B.; Cosgriff-Hernandez, E. Effects of humidity and solution viscosity on electrospun fiber morphology. *Tissue Eng., Part C* **2013**, *19* (10), 810−9.
(58) He, Y.; Yang, F. F.; Zhao, H. M.; Gao, Q.; Xia, B.; Fu, J. Z. Research on the printability of hydrogels in 3D bioprinting. *Sci. Rep.* **2016**, *6*, 29977.
(59) Khorshidi, S.; Solouk, A.; Mirzadeh, H.; Mazinani, S.; Lagaron, J. M.; Sharifi, S.; Ramakrishna, S. A review of key challenges of electrospun scaffolds for tissue-engineering applications. *J. Tissue Eng. Regener. Med.* **2016**, *10* (9), 715−38.
(60) O'Hare, K. D.; Spedding, P. L.; Grimshaw, J. Evaporation of the Ethanol and Water Components Comprising a Binary Liquid Mixture. *Dev. Chem. Eng. Miner. Process.* **1993**, *1* (2−3), 118−128.
(61) Park, S. N.; Park, J. C.; Kim, H. O.; Song, M. J.; Suh, H. Characterization of porous collagen/hyaluronic acid scaffold modified by 1-ethyl-3-(3-dimethylaminopropyl)carbodiimide cross-linking. *Biomaterials* **2002**, *23* (4), 1205−12.
(62) Achterberg, V. F.; Buscemi, L.; Diekmann, H.; Smith-Clerc, J.; Schwengler, H.; Meister, J. J.; Wenck, H.; Gallinat, S.; Hinz, B. The nano-scale mechanical properties of the extracellular matrix regulate dermal fibroblast function. *J. Invest. Dermatol.* **2014**, *134* (7), 1862−1872.
(63) Chen, E. J.; Novakofski, J.; Jenkins, W. K.; O'Brien, W. D. Young's modulus measurements of soft tissues with application to elasticity imaging. *IEEE Trans. Ultrason., Ferroelect., Freq. Contr.* **1996**, *43* (1), 191−194.
(64) Rosales, A. M.; Anseth, K. S. The design of reversible hydrogels to capture extracellular matrix dynamics. *Nat. Rev. Mater.* **2016**, *1*, 15012.
(65) Galiano, R. D.; Michaels, J.; Dobryansky, M.; Levine, J. P.; Gurtner, G. C. Quantitative and reproducible murine model of excisional wound healing. *Wound Repair Regen.* **2004**, *12* (4), 485−492.
(66) Burck, J.; Heissler, S.; Geckle, U.; Ardakani, M. F.; Schneider, R.; Ulrich, A. S.; Kazanci, M. Resemblance of electrospun collagen nanofibers to their native structure. *Langmuir* **2013**, *29* (5), 1562−72.
(67) Pasquinelli, G.; Vinci, M. C.; Gamberini, C.; Orrico, C.; Foroni, L.; Guarnieri, C.; Parenti, A.; Gargiulo, M.; Ledda, F.; Caldarera, C. M.; Muscari, C. Architectural organization and functional features of early endothelial progenitor cells cultured in a hyaluronan-based polymer scaffold. *Tissue Eng., Part A* **2009**, *15* (9), 2751−62.
(68) Barnes, C. P.; Sell, S. A.; Boland, E. D.; Simpson, D. G.; Bowlin, G. L. Nanofiber technology: designing the next generation of tissue engineering scaffolds. *Adv. Drug Delivery Rev.* **2007**, *59* (14), 1413−33.
(69) Loh, Q. L.; Choong, C. Three-dimensional scaffolds for tissue engineering applications: role of porosity and pore size. *Tissue Eng., Part B* **2013**, *19* (6), 485−502.

DOI: 10.1021/acsami.9b17322
ACS Appl. Mater. Interfaces XXXX, XXX, XXX−XXX